A thermodynamically consistent cohesive-frictional interface model for mixed mode delamination

Francesco Parrinello[a,*], Giuseppe Marannano[b], Guido Borino[a,]

[a]*Dipartimento di Ingegneria Civile, Ambientale, Aerospaziale, dei Materiali.
Università di Palermo, Viale delle Scienze, Ed. 8, 90128 Palermo*
[b]*Dipartimento di Ingegneria Chimica, Gestionale, Informatica, Meccanica.
Università di Palermo, Viale delle Scienze, Ed. 8, 90128 Palermo*

Abstract

A new interface constitutive model based on damage mechanics and frictional plasticity theory is presented. The model is thermodynamically consistent, it is able to accurately reproduce arbitrary mixed mode debonding conditions and it is proved that the separation work is always bounded between the fracture energy in mode I and the fracture energy in mode II. Analytical results are given for proportional loading paths and for two non-proportional loading paths, confirming the correct behaviour of the model for complex loading histories. Numerical and analytical solutions are compared for three classical delamination tests and frictional effects on 4ENF are also considered.

Keywords:

cohesive-frictional interface, mixed-mode delamination, thermodynamics.

1. Introduction

The challenge of modeling the progressive formation, development and propagation of displacement discontinuities, such as fracture or delamination phenomena, has been successfully faced by the introduction of Cohesive Zone Models (CZMs). CZMs are constitutive non-linear relations able to model the tran-

*corresponding author
Email addresses: `francesco.parrinello@unipa.it` (Francesco Parrinello),
`giuseppe.marannano@unipa.it` (Giuseppe Marannano), `guido.borino@unipa.it` (Guido Borino)

sition between virgin material, partially broken ligaments and full opening along a surface. The first pioneering papers goes back to the early 60s by Dugdale (1960) and Barenblatt (1962) who established the physical basis of the constitutive framework. Since then many developments have been done, with the main assessment of joining the surface cohesive constitutive model with the concept of interface elements (Xu and Needleman, 1993; Allix et al., 1995; Alfano and Crisfield, 2001). The introduction of non-linear interface elements in conjunction with standard Finite Element analysis gave rise to one of the most powerful approach to non-linear structural failure analysis.

In the last years, several crucial aspects have been accurately investigated such as: isotropic and orthotropic cohesive interface models (Corigliano and Allix, 2000), coupling damage and plasticity (Spada et al., 2009; Kolluri et al., 2014), different mode I and mode II fracture energies (Alfano and Crisfield, 2001; Benzerga et al., 2008), thermodynamic consistency (Parrinello et al., 2009; Mosler and Scheider, 2011; Guiamatsia and Nguyen, 2014; Serpieri et al., 2015), time dependent and viscous effects (Corigliano and Ricci, 2001; Giambanco and Fileccia Scimemi, 2006; Zreid et al., 2013; Musto and Alfano, 2013)

Recently, special attention has been focused on the assessment of an energy rational behavior of interfaces models loaded under arbitrary mixed mode conditions. It is actually required a physical sound behavior for monotonic and cyclic loading for different mixity rate loadings. It is also of paramount interest to ensure, for any loading path, the satisfaction of thermodynamic principles.

In order to control mixed loading in traction and shearing Park et al. (2009) proposed a potential-based cohesive zone model for mixed-mode fracture, which is defined as a particle debonding potential at the material point level. The model is based on a unique potential which is function of both normal and tangential component of the separation displacement. The work of separation is evaluated for some loading paths, producing physically consistent results. On the contrary, Park et al. (2009) show that, when the mode I and mode II fracture energies are $G_{II} > G_I$, the potential based of Xu and Needleman (1993) produces work of separation, W_T, in a mixed mode loading paths

which is $W_T > G_{II} > G_I$, in disagreement with experimental evidence (see Benzeggagh and Kenane (1996)). Analogously, when $G_{II} < G_I$, the separation work in a mixed mode loading path is $W_T < G_{II} < G_I$.

McGarry et al. (2014) analyze potential and non-potential based models for mixed mode separation loading paths and under over-closure conditions showing some shortcoming of the model of Xu and Needleman (1993).

Dimitri et al. (2014) carefully evaluate the response performances of four well-known interface constitutive models under mixed mode loading and whether they are always consistent in terms of stress and energy dissipation. In Dimitri et al. (2014), the authors show that the CZMs proposed by McGarry et al. (2014); Högberg (2006); Camanho et al. (2003), under particular mixed loading condition, may produce unphysical results. Moreover, in the model of van den Bosch et al. (2006) the unloading law, different than the loading one, is not explicitly defined and energy dissipation can not be directly evaluated. In such model two independent laws are defined respectively for the tangential traction component and for the normal one and, as already stated in Mosler and Scheider (2011), symmetry the tangent stiffness matrix is not achieved.

On the basis of the above criticism, Dimitri et al. (2014) propose a thermodynamically consistent model, defined as an improvement of the van den Bosch et al. (2006) model, but derived by an Helmholtz free energy function. The same tangential and normal traction interface laws of van den Bosch et al. (2006) are rigorously derived by applying the Coleman and Noll (1963) procedure. The cost of such achievement is the necessity of employ four independent scalar damage variables. Mosler and Scheider (2011) pointed out the relevance of the thermodynamical consistency for finite strains and anisotropic interface models.

In Serpieri et al. (2015) a thermodynamic consistent cohesive frictional model with different mode I and mode II fracture energies is presented. The model is defined by means of a single scalar damage variable and a single scalar equivalent displacement. The authors prove, that under the above hypothesis the total dissipation of energy, which is equal to the separation work, in pure mode I (G_I)

3

68 and in pure mode II (G_{II}) has to be the same, that is $G_I = G_{II}$. Moreover,
69 the authors ascribe the greater mode II fracture energy G_{II} with respect to G_I,
70 which is an experimental evidence, to frictional effects, and they state that such
71 effects are always present at the mesoscale level.

72   The possibility to have an interface model which can reproduce a smooth
73 transition between cohesive and frictional deformation modes has been presented
74 in several papers (see e.g. Ganghoffer and Schultz (1997); Alfano and Sacco
75 (2006); Parrinello et al. (2009); Spada et al. (2009); Sacco and Lebon (2012);
76 Guiamatsia and Nguyen (2014)). The contribution of frictional behaviour to the
77 the mode II dissipation energy has been analyzed under increasing cycling load
78 in Parrinello et al. (2013) by the cohesive-frictional interface model proposed in
79 Parrinello et al. (2009).

80   The availability of a model with a single scalar damage variable, thermody-
81 namically consistent, with two different fracture energies in mode I and in mode
82 II, which behaves also correctly under any cyclic loading in mixed mode, is, in
83 the authors' knowledge, a goal not yet reached.

84   In the present paper a new thermodynamically consistent CZM is proposed.
85 It is based on a predefined Helmholtz free energy density with a single scalar
86 damage variable and it produces two independent work of separation in pure
87 mode I and pure mode II delamination conditions. The proposed model can also
88 take in to account frictional effects with a smooth transition of the mechanical
89 behavior, from the initial elastic one of the virgin material, to the fully debonded
90 behavior with frictional residual strength. The cohesive-frictional behavior is
91 based on the same mesoscale interpretation of the scalar damage variable, pre-
92 viously proposed in Alfano and Sacco (2006); Parrinello et al. (2009). In fact,
93 the model proposed in this paper can be considered as a rational evolution of
94 the interface model developed by Parrinello et al. (2009), whose main limit is
95 that it produces a unique separation work, excluding the presence of frictional
96 effects, independently of the debonding mode condition. The proposed formu-
97 lation is defined by a new damage activation function. Traction components,
98 damage evolution and the relevant constitutive equations are derived by follow-

ing classical thermodynamic arguments (Coleman and Noll, 1963). The model implicitly verify the second thermodynamic law by proving that dissipation is non-negative for every loading path; it produces two independent fracture energies in pure mode I and pure mode II debonding conditions and produces physically consistent results under mixed mode debonding ones.

The paper is organized as follows: the new model is presented in Section 2. The solutions of monotonic and non-proportional loading paths are analytically derived in respectively in Section 3 and in Section 4. Numerical results of three delamination tests are compared with the relevant analytical solutions in Section 5 and, finally, closing remarks are reported in section 6.

2. The cohesive-frictional model with different fracture energy in mode I and in mode II

Damage mechanics concepts are widely used for cohesive interface models (Corigliano, 1993; Daudeville et al., 1995; Allix et al., 1995; Corigliano and Allix, 2000; Mosler and Scheider, 2011) since they possess all the necessary features to properly describe cohesive fracture processes.

As recently pointed out for damage based interface constitutive models (Alfano and Sacco, 2006; Parrinello et al., 2009; Spada et al., 2009; Serpieri and Alfano, 2011; Guiamatsia and Nguyen, 2014) effective formulations can be derived considering the classical scalar damage variable ω in a geometrical setting as

$$\omega := \frac{\mathrm{d}S_c}{\mathrm{d}S} = \frac{\mathrm{d}S - \mathrm{d}S_s}{\mathrm{d}S} \tag{1}$$

where, at a generic point, the reference interface surface $\mathrm{d}S$ is associated to a sound (virgin) fraction, $\mathrm{d}S_s$ and to a complementary cracked fraction $\mathrm{d}S_c$ (see Figure 1 a))

Adopting a mixture approach, at the sub-scale where the two fractions are defined, a specific kinematic, static and constitutive relations can be established, which are then reported at the macro interface level. Since interface are used to
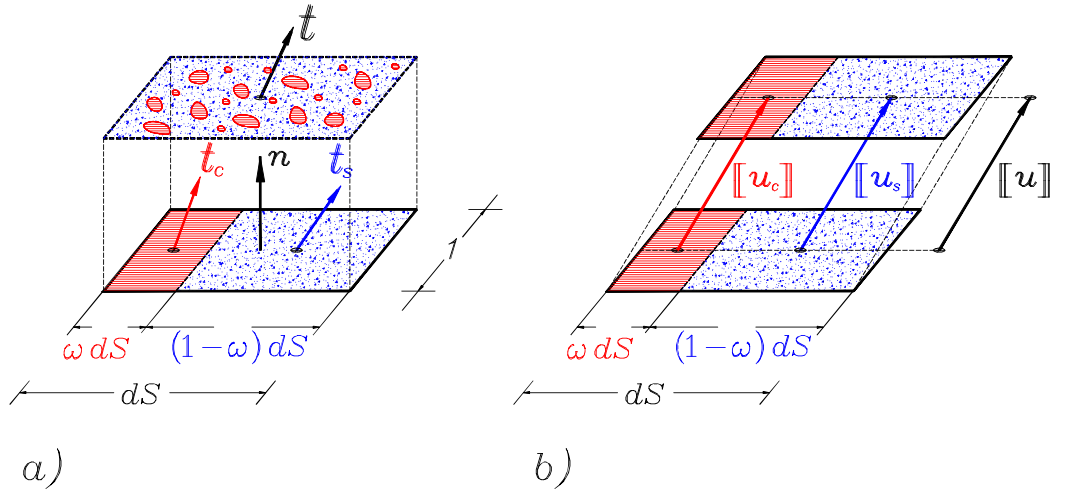
Figure 1: Geometrical sketch showing the decomposition in two fractions: a) Decomposition of the damaged surface dS in the cracked fraction $\omega\,dS$ and the sound fraction $(1-\omega)\,dS$ with the respective traction vectors $\boldsymbol{t}_c$ and $\boldsymbol{t}_s$. By the equilibrium condition $\boldsymbol{t}_s + \boldsymbol{t}_c = \boldsymbol{t}$. b) kinematic representation of the displacement jump $[\![\boldsymbol{u}]\!]$, with $[\![\boldsymbol{u}_c]\!]$ and $[\![\boldsymbol{u}_s]\!]$ jump displacement vectors across the cracked and the sound fractions. By kinematic consistency $[\![\boldsymbol{u}]\!] = [\![\boldsymbol{u}_c]\!] = [\![\boldsymbol{u}_s]\!]$.

drive decohesion along a prefixed zero-thickness surface, the kinematic variable adopted to measure the actual deformation is the displacement jump vector across the interface, namely $[\![\boldsymbol{u}]\!] = \boldsymbol{u}^+ - \boldsymbol{u}^-$, where $\boldsymbol{u}^+$ and $\boldsymbol{u}^-$ are the displacement vector at the upper $(+)$ and lower $(-)$ side of the interface. Moreover, in order to simplify the notation, we write the displacement jump without the brackets, i.e. $[\![\boldsymbol{u}]\!] := \boldsymbol{u}$.

Since the present approach is based on a mixture theory with two fractions, it is allowed to define for each fraction a specific displacement jump vector, $[\![\boldsymbol{u}_c]\!] := \boldsymbol{u}_c$ and $[\![\boldsymbol{u}_s]\!] := \boldsymbol{u}_s$, where the indexes c and s stands for *cracked* and *sound* fraction (see Figure 1 b)).

The internal kinematic consistency requires that each strain measure of the two fractions has to be equal to the global displacement jump, namely

$$\boldsymbol{u} = \boldsymbol{u}_c = \boldsymbol{u}_s \qquad (2)$$

Having in mind the different constitutive relation to adopt for each fraction, it is convenient to introduce a specific additive decomposition which account for elastic and inelastic deformations. Namely:

For the *Sound fraction* no inelastic deformation develops and only elastic component is considered

$$\boldsymbol{u}_s = \boldsymbol{\delta}_s^e \qquad (3)$$

For the *Cracked fraction* the total deformation is considered as the sum of three different contributions, namely:

$$\boldsymbol{u}_c = \boldsymbol{\delta}_c^e + \boldsymbol{\delta}_c^p + \boldsymbol{\delta}_c^d \qquad (4)$$

where $\boldsymbol{\delta}_c^e$ is the elastic component (due to micro elastic deformation modes in contact and/or in sliding), $\boldsymbol{\delta}_c^p$ is the plastic component (due to to frictional deformation modes including dilatancy), and $\boldsymbol{\delta}_c^d$ is the detachment component or gap vector (due to opening or even sliding without compressive state).

The displacement jump contributions defined in Eq. (4) have also to satisfy some kinematic conditions related to the unilateral contact (for opening/closing

7

conditions), as well as for frictional effects. All the components jump vectors have a Cartesian component along the normal to the interface oriented from the $(-)$ lower surface to the $(+)$ upper surface, which is denoted by an extra index n, and a tangential component along the interface denoted by an extra index t.

Considering the cracked fraction, the normal elastic component δ_{cn}^e has to be non-positive, since it is active only in a contact compressive state. Conversely, the detachment normal component, δ_{cn}^d, has to be non-negative, since it describe the opening mechanism. Moreover, the two quantities δ_{cn}^e and δ_{cn}^d cannot be both different from zero at the same time. As a conclusion the following classic elastic contact complementarity conditions holds

$$\delta_{cn}^e \leq 0, \qquad \delta_{cn}^d \geq 0, \qquad \delta_{cn}^e \, \delta_{cn}^d = 0 \tag{5}$$

Considering the elastic tangential component, δ_{ct}^e, it is observed that no sign restriction is required, but it has also to satisfy the mutual activation condition in the form

$$\delta_{ct}^e \, \delta_{cn}^d = 0. \tag{6}$$

Finally, no sign restriction are imposed on the detachment tangential component $\boldsymbol{\delta}_{ct}^d$, which means that in case of re-closing deformation mode tangential components previously produced in a opening state, may be accounted for, $(\delta_{ct}^d \neq 0)$.

As a final remark, it can be easily proved that Eqs. (2)–(6) hold also if written in rate form.

2.1. Thermodynamic consistency

In order to comply thermodynamic principles, the Helmholtz free energy density function (for unit surface) is introduced, playing the role of potential with respect to the state variables, either external, or internal ones. Since the adopted model is based on the superposition of two fractions, in which the sound fraction is weighted by the integrity coefficient $(1 - \omega)$, whereas the cracked fraction is weighted by the damage coefficient ω, it follows that the Helmholtz free energy can be given in the following form:

8

$$\psi(\boldsymbol{\delta}_s^e, \boldsymbol{\delta}_c^e, \omega, \xi) = (1-\omega)\bar{\psi}_s^e(\boldsymbol{\delta}_s^e) + \omega\bar{\psi}_c^e(\boldsymbol{\delta}_c^e) + \psi_i(\xi) \tag{7}$$

where $\bar{\psi}_s^e$ and $\bar{\psi}_c^e$ are the elastic free energy densities for the unweighted sound and cracked fractions, both function of the respective elastic deformations. ψ_i is the internal free energy related to a scalar internal variable ξ, introduced for a specific description of the post-peak traction – relative displacement regime (softening).

In what follow linear elasticity behavior is assumed, either for the sound, or for the cracked fraction, which implies a quadratic form for the two elastic free energies, namely

$$\bar{\psi}_s^e(\boldsymbol{\delta}_s^e) = \frac{1}{2}\boldsymbol{\delta}_s^{eT}\boldsymbol{K}_s\boldsymbol{\delta}_s^e; \qquad \bar{\psi}_c^e(\boldsymbol{\delta}_c^e) = \frac{1}{2}\boldsymbol{\delta}_c^{eT}\boldsymbol{K}_c\boldsymbol{\delta}_c^e; \tag{8}$$

Equations (8) give the stored strain energies of the two fractions each of which, in agreement with Eq. (7), is weighted by the coefficients $(1-\omega)$ and ω respectively.

$\boldsymbol{K}_s$ and $\boldsymbol{K}_c$ are two positive definite diagonal stiffness matrices in which K_i^s and K_i^c are positive stiffness coefficients and the index $(i = n, t)$ stands for normal and tangential component.

Thermodynamic consistency, in the form of the second principle, can be enforced by the Clausius-Duhem inequality, which gives an explicit form for the non-negative mechanical energy dissipation density:

$$D = \boldsymbol{t}^T \ \dot{\boldsymbol{u}} - \dot{\psi} \geq 0 \tag{9}$$

Expanding $\dot{\psi}$, considering the specific form given in Eqs. (7) and (8), and making also use of the decomposition of the total interface strains, given in Eqs. (3) and (4) written in the following rate form: $\dot{\boldsymbol{\delta}}_s^e = \dot{\boldsymbol{u}}$ and $\dot{\boldsymbol{\delta}}_c^e = \dot{\boldsymbol{u}} - \dot{\boldsymbol{\delta}}_c^p - \dot{\boldsymbol{\delta}}_c^d$, gives

$$D = \left(\boldsymbol{t} - \frac{\partial\psi}{\partial\boldsymbol{\delta}_s^e} - \frac{\partial\psi}{\partial\boldsymbol{\delta}_c^e}\right)^T \dot{\boldsymbol{u}} + \left(\frac{\partial\psi}{\partial\boldsymbol{\delta}_c^e}\right)^T \left(\dot{\boldsymbol{\delta}}_c^p + \dot{\boldsymbol{\delta}}_c^d\right) - \frac{\partial\psi}{\partial\omega}\dot{\omega} - \frac{\partial\psi_{in}}{\partial\xi}\dot{\xi} \geq 0. \tag{10}$$

No dissipation ($D = 0$) is produced in the case of any purely reversible deformation modes (elasticity) in which $\dot{\omega} = \dot{\xi} = 0$ and $\dot{\boldsymbol{\delta}}_c^p = \dot{\boldsymbol{\delta}}_c^d = \boldsymbol{0}$, which gives as

9

result

$$\boldsymbol{t} = \underbrace{\frac{\partial \psi}{\partial \boldsymbol{\delta}_s^e}}_{\boldsymbol{t}_s} + \underbrace{\frac{\partial \psi}{\partial \boldsymbol{\delta}_c^e}}_{\boldsymbol{t}_c} \tag{11}$$

where it has been set

$$\boldsymbol{t}_s := \frac{\partial \psi}{\partial \boldsymbol{\delta}_s^e} = (1 - \omega)\boldsymbol{K}_s \boldsymbol{\delta}_s^e; \qquad \boldsymbol{t}_c := \frac{\partial \psi}{\partial \boldsymbol{\delta}_c^e} = \omega \boldsymbol{K}_c \boldsymbol{\delta}_c^e \tag{12}$$

The two tractions, $\boldsymbol{t}_s$ and $\boldsymbol{t}_c$ (See Figure 1 a) play the role of traction vectors acting on each of the two fractions of the model and the relation $\boldsymbol{t} = \boldsymbol{t}_s + \boldsymbol{t}_c$ is a form of internal linear momentum balance equation.

Following a well established procedure, the state equation (11) holds also for dissipative deformation processes, so that the dissipation function can be rewritten as

$$D = Y\dot{\omega} + \boldsymbol{t}_c^T \dot{\boldsymbol{\delta}}_c^p - \chi\dot{\xi} \geq 0. \tag{13}$$

where the orthogonality condition $\boldsymbol{t}_c^T \dot{\boldsymbol{\delta}}_c^d = 0$ has been used. The energy release rate Y and the static like conjugate internal variable χ introduced in Eq. (13) complete the set of state equations defined as

$$\begin{aligned} Y &= -\frac{\partial \psi}{\partial \omega} = \bar{\psi}_s^e - \bar{\psi}_c^e \\ &= \frac{1}{2}\boldsymbol{\delta}_s^{eT}\boldsymbol{K}_s\boldsymbol{\delta}_s^e - \frac{1}{2}\boldsymbol{\delta}_c^{eT}\boldsymbol{K}_c\boldsymbol{\delta}_c^e \end{aligned} \tag{14}$$

and

$$\chi := \frac{\partial \psi_i}{\partial \xi} \tag{15}$$

Equation (13) states that the total dissipation D is given by a first term related to the energy for a possible increment of damage $Y\dot{\omega}$, a second term for a possible frictional mechanism $\boldsymbol{t}_c^T \dot{\boldsymbol{\delta}}_c^p$ (including dilatancy effects) and finally the third (negative) term $\chi\dot{\xi}$ is the rate energy spent in the reorganizing the internal microstructure for the evolution of the softening behavior. Moreover, observing Eq. (14) it can be stated that the energy release rate Y is given as the strain energy in the sound fraction minus the strain energy of the cracked fraction, the latter being not available for further damage increments.

10

A further relevant feature shown by Eq.(13) is that there are no dissipative interactions between damage and friction modes. This uncoupled structure means that a damage increment (decohesion growth) does not necessarily requires a change in the frictional state and, of course, the vice-versa. Equation (13) can then be split as

$$D = D_d + D_p \qquad (16)$$

where D_d and D_p are the dissipation functions related to damage and to frictional increment, given as

$$
\begin{aligned}
D_d(\dot{\omega}, \dot{\xi}) &= Y\dot{\omega} - \chi\dot{\xi} \geq 0 \\
D_p(\dot{\boldsymbol{\delta}}_c^p) &= \boldsymbol{t}_c^T \dot{\boldsymbol{\delta}}_c^p \geq 0
\end{aligned}
\qquad (17)
$$

The structure of the dissipation split in two term suggests the introduction of two distinct activation criteria which drive damage and friction activation as well as the related flow rules.

2.2. Activation functions and flow rules

In order to derive an activation function able to properly describe mode I (opening), mode II (sliding) and all the possible mixed modes, the following interface damage activation condition is considered:

$$\phi_d(Y, \chi; \boldsymbol{u}) = Y - \chi - \bar{Y}(\boldsymbol{u}) - Y_0 \leq 0 \qquad (18)$$

in which Y_0 is a positive constant value accounting for the initial unloaded damage threshold; the internal variable χ describes the damage threshold increment, $\dot{\chi} \geq 0$ due to the damage evolution, and finally $\bar{Y}(\boldsymbol{u})$ is a positive term given as function of the kinematic state

$$\bar{Y}(\boldsymbol{u}) = \frac{1}{2}\boldsymbol{u}^T \boldsymbol{A}\boldsymbol{u} = \frac{1}{2}A_n u_n^2 + \frac{1}{2}A_t u_t^2 \qquad (19)$$

where $\boldsymbol{A}$ is a positive definite diagonal matrix collecting two positive constitutive parameters $A_n \geq 0$ and $A_t \geq 0$. The associated flow rules and loading-unloading

11

conditions can be obtained as

$$\dot{\omega} = \frac{\partial \phi_d}{\partial Y} \dot{\lambda}_d = \dot{\lambda}_d,$$
$$\dot{\xi} = -\frac{\partial \phi_d}{\partial \chi} \dot{\lambda}_d = \dot{\lambda}_d, \tag{20}$$
$$\dot{\lambda}_d \geq 0, \quad \phi_d \dot{\lambda}_d = 0, \quad \dot{\phi}_d \dot{\lambda}_d = 0$$

where $\dot{\lambda}_d$ is the damage multiplier.

Unlike what presented previously by the authors (Parrinello et al., 2009), where the damage activation function is driven only by Y, producing the same separation work in pure model I, in mode II and for any mixed mode, in the present paper a new formulation is proposed, which is enhanced by the insertion of a state displacement dependent damage activation function, as shown by Eq.(18). This new approach, even if still based on a single scalar damage variable, produces a different separation work in pure mode I and in pure mode II, and as it will be shown in the next Section does not suffer of any inconsistency in mixed modes. The values of the two new constitutive parameters, A_n and A_t, are related to the values of the Fracture Energies, G_I and G_{II}. If it is assumed $G_{II} > G_I$, as it is usually shown by experimental evidences, it is necessary to set $A_t > A_n$. Otherwise, in the case of $G_I > G_{II}$ the parameters have to be set as $A_n > A_t$. Details on choice and on the physical meaning of the two constants will be given in the next Section.

The dissipation associated with the damage activation can be computed considering that the flow rules shows $\dot{\omega} = \dot{\lambda}_d > 0$ only if $\phi_d = 0$, which considering the first of Eq.(17) gives

$$D_d = Y\dot{\omega} - \chi\dot{\xi} = \left(\frac{1}{2}A_n u_n^2 + \frac{1}{2}A_t u_t^2 + Y_0\right)\dot{\lambda}_d \geq 0 \tag{21}$$

showing the unconditioned positiveness of the dissipation rate for any damage increment, being $D_d = 0$ only if $\dot{\lambda}_d = 0$.

Finally, in order to prevent damage activation under pure compressive stress state, normal stiffness of the sound fraction and normal stiffness of the cracked fraction are imposed to be equal, that is $K_n^s = K_n^c$. In fact, for a displacement

12

$u_n < 0$ and $u_t = 0$, and assuming null plastic deformation $\boldsymbol{\delta}_c^p = \mathbf{0}$, the relevant energy release rate is

$$Y = \frac{1}{2} K_n^s u_n^2 - \frac{1}{2} K_n^c u_n^2 = 0, \tag{22}$$

and no damage increment is achieved.

Activation function and flow rules for the plastic displacement jump $\dot{\boldsymbol{\delta}}_c^p$ are achieved in the framework of non-associative plasticity theory. The activation function has the form of the classical Mohr-Coulomb yield function

$$\phi_p(\boldsymbol{t}_c) = |t_{ct}| + \alpha t_{cn} \leq 0 \tag{23}$$

and by means of the following plastic potential

$$\Omega_p(\boldsymbol{t}_c) = |t_{ct}| + \beta t_{cn} \leq 0 \tag{24}$$

where t_{cn} and t_{ct} are the normal and tangential components of the traction vector $\boldsymbol{t}_c$; α and β, with $\alpha \geq \beta$ are the frictional and the dilatancy coefficients respectively. The plastic (or frictional) flow rules and the loading/unloading conditions read

$$
\begin{aligned}
\dot{\delta}_n^p &= \frac{\partial \Omega_p}{\partial t_{cn}} \dot{\lambda}_p = \mathrm{sgn}(t_{ct}) \dot{\lambda}_p, \\
\dot{\delta}_t^p &= \frac{\partial \Omega_p}{\partial t_{ct}} \dot{\lambda}_p = \beta \dot{\lambda}_p, \\
\dot{\lambda}_p &\geq 0, \quad \phi_p \dot{\lambda}_p = 0, \quad \dot{\phi}_p \dot{\lambda}_p = 0
\end{aligned}
\tag{25}
$$

The dissipation rate associated with frictional active mechanisms is evaluated considering that $\dot{\lambda}_p > 0$ only if $\phi_p = 0$ which, considering the second of the Eqs.(17), gives

$$D_p = \boldsymbol{t}_c^T \dot{\boldsymbol{\delta}}^p = (|t_{ct}| + \beta t_{cn}) \dot{\lambda}_p \geq (|t_{ct}| + \alpha t_{cn}) \dot{\lambda}_p = 0 \tag{26}$$

which shows that dissipation is always positive for any frictional rate displacement rate, with $D_p = 0$ only if $\dot{\lambda}_p = 0$

The cohesive model is then completed by the state laws for the internal variable χ which drive the damage evolution law. In case of simple linear softening

in normal traction-opening displacement (mode I), it can be shown that internal free energy and internal state law read:

$$\psi_i(\xi) = G_I \frac{u_e}{u_f} \left(\frac{u_f^2/(u_f - u_e)}{u_f(1 - \xi) + u_e \xi} - \xi \right)$$

$$\chi(\xi) := \frac{d\psi_i(\xi)}{d\xi} = G_I \frac{u_e}{u_f} \left[\left(\frac{u_f}{u_f(1 - \xi) + u_e \xi} \right)^2 - 1 \right]$$

(27)

where u_e and u_f are the separation displacements for the limit elastic threshold and for the full damage condition ($\omega = 1$, i.e. full detachment) in pure mode I opening condition, $G_I = 1/2 K_n^s u_e u_f$ is the fracture energy in mode I and finally, K_n^s is the stiffness normal component of the interface sound fraction. As far as the other material parameters are concerned, it is set

$$Y_0 = \frac{1}{2} K_n^s u_e^2 \equiv G_I \frac{u_e}{u_f}$$

$$A_t = K_t^s \left(1 - \frac{G_I}{G_{II}} \right); \qquad A_n = 0$$

(28)

The two constants A_n and A_t have been fixed under the condition that the fracture energy in mode II (G_{II}) is greater than the fracture energy in mode I (G_I), i.e. $G_{II} > G_I$. Finally, the relations in Eqs.(28) among the fracture energies and the parameters Y_0 and A_t will be explained in detail in Sect. 3.

3. Monotonic loading paths

In this Section the monotonic mixed delamination path, represented in Figure 2 for a linear interface element, is analyzed. The displacement jump $\boldsymbol{u}$ is decomposed in the local Cartesian components as

$$\boldsymbol{u} = u_t \boldsymbol{e}_t + u_n \boldsymbol{e}_n = u \cos \gamma \, \boldsymbol{e}_t + u \sin \gamma \, \boldsymbol{e}_n$$

(29)

where $u = (\boldsymbol{u}^T \boldsymbol{u})^{1/2}$ and $\boldsymbol{e}_t$, and $\boldsymbol{e}_n$ are the unit tangential and normal vectors to the interface plane.

The pure mode I delamination condition is produced by a loading angle $\gamma = \pi/2$ and the pure mode II delamination condition is obtained by assuming a loading angle $\gamma = 0$.

14

The imposed displacement $\boldsymbol{u}$ monotonically increases up to the complete
interface delamination. The same problem is analyzed in Park et al. (2009)
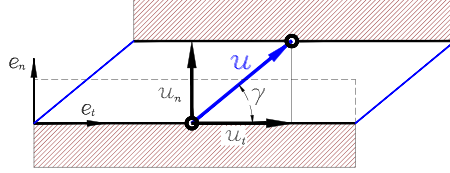where the separation work is computed for some significant values of angle γ.

Figure 2: Monotonic mixed mode loading scheme. The displacement jump $\boldsymbol{u}$ decomposed as $\boldsymbol{u} = u_t \boldsymbol{e}_t + u_n \boldsymbol{e}_n$.

The separation work $W = W_n + W_t$ can be defined as the sum of two different
contributions, namely: the normal separation work W_n and the tangential one
W_t, which are mathematically defined as

$$
\begin{aligned}
W_n &= \int_0^{+\infty} t_n(\gamma, \boldsymbol{u}) \, \mathrm{d}u_n \\
W_t &= \int_0^{+\infty} t_t(\gamma, \boldsymbol{u}) \, \mathrm{d}u_t
\end{aligned}
\tag{30}
$$

Due to the assumed non-negative opening displacement ($u_n \geq 0$), the frictional
traction has not to be considered, as well as its effect on the separation work.
Traction components are

$$
\begin{aligned}
t_n &= (1 - \omega) K_n^s \, u \, \sin(\gamma) \\
t_t &= (1 - \omega) K_t^s \, u \, \cos(\gamma)
\end{aligned}
\tag{31}
$$

The initial interface behavior is elastic with null damage and null internal vari-
able ($\omega = 0$ and $\xi = 0$) and the maximum elastic traction is reached when
the damage activation condition is attained $\phi_d(Y, u_t, \chi) = 0$, where $\chi(0) = 0$,
$A_n = 0$, $A_t > 0$ and the energy release rate is

$$
Y = \frac{1}{2} K_n^s \, u^2 \, \sin^2(\gamma) + \frac{1}{2} K_t^s \, u^2 \, \cos^2(\gamma),
\tag{32}
$$

15

therefore

$$\phi_d\left(Y, u_t, \chi\right) = Y - \chi\left(\xi\right) - \frac{1}{2}A_t u_t^2 - Y_0 =$$
$$= \frac{1}{2}K_n^s u^2 \sin^2(\gamma) + \frac{1}{2}(K_t^s - A_t)u^2 \cos^2(\gamma) - Y_0 = \qquad (33)$$
$$= \frac{1}{2}\frac{K_n^s u^2}{C^2(\gamma)} - Y_0 = 0$$

where

$$C(\gamma) = \left(\sin^2(\gamma) + \frac{K_t^s - A_t}{K_n^s}\cos^2(\gamma)\right)^{-1/2} \qquad (34)$$

is a loading angle dependent function. For $\gamma = \pi/2$ (opening in mode I) $C(\pi/2) = 1$, whereas for $\gamma = 0$ (sliding in mode II) $C(0) = \sqrt{K_n^s/(K_t^s - A_t)}$.

By substitution of the first of Eqs. (28) in Eq. (33), the imposed separation displacement $\bar{u}_e$ at the limit elastic is

$$\bar{u}_e = u_e\, C(\gamma) \qquad (35)$$

The linear-elastic branch is followed by a descending (softening) one with increasing damage and, in virtue of flow rules of Eqs. (20), damage activation function (18) and softening law (27), kinematic internal variable and damage variable are

$$\xi = \omega = \frac{u_f}{u_f - u_e}\left[1 - \frac{u_e}{u}C(\gamma)\right] \qquad (36)$$

and separation displacement $\bar{u}_f$ at the fully damaged condition ($\omega = 1$) is

$$\bar{u}_f = u_f\, C(\gamma) \qquad (37)$$

The traction components at the descending branch are obtained from Eqs. (31) and (36)

$$t_n(u, \gamma) = \frac{u_f u_e\, C(\gamma) - u_e u}{u_f - u_e}K_n^s \sin(\gamma)$$
$$t_t(u, \gamma) = \frac{u_f u_e\, C(\gamma) - u_e u}{u_f - u_e}K_t^s \cos(\gamma). \qquad (38)$$

The work done by normal traction and the work done by tangential one can be computed by Eqs. (30) and are

$$W_n(\gamma) = \frac{1}{2}K_n^s\, u_e u_f\, C^2(\gamma)\sin^2(\gamma),$$
$$W_t(\gamma) = \frac{1}{2}K_t^s\, u_e u_f\, C^2(\gamma)\cos^2(\gamma). \qquad (39)$$

16

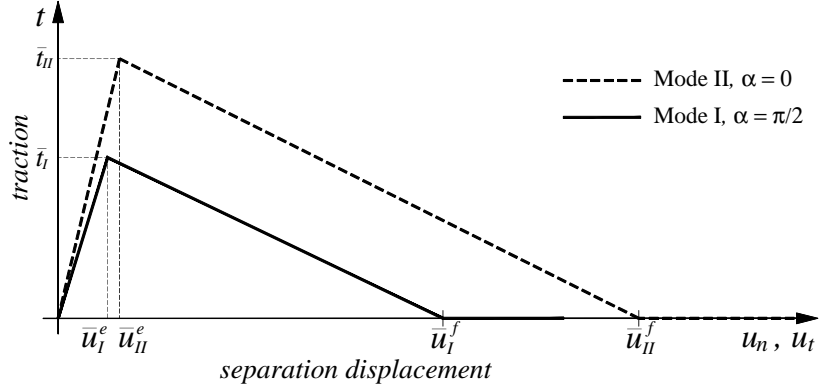In Figure (3) the qualitatively response of the interface subjected to the mono-

Figure 3: Mode I response and mode II response for monotonic loading path.

330

331 tonic loading path is represented in terms of traction *vs* separation displacement

332 for the two limit cases of pure mode I and pure mode II.

333 In the pure mode I debonding condition ($\gamma = \pi/2$) limit elastic displacement

334 $\bar{u}_I^e$, the fully debonding displacement $\bar{u}_I^f$ and the maximum normal traction $\bar{t}_I$,

335 respectively are

$$\bar{u}_I^e = u_e$$
$$\bar{u}_I^f = u_f \qquad (40)$$
$$\bar{t}_I = K_n^s u_e,$$

336 whereas, in the pure mode II debonding condition ($\gamma = 0$) limit elastic displace-

337 ment $\bar{u}_{II}^e$, fully debonding displacement $\bar{u}_{II}^f$ and maximum normal traction $\bar{t}_{II}$,

17

respectively are

$$\bar{u}_{II}^e = \sqrt{\frac{K_n^s}{K_t^s - A_t}}\, u_e$$

$$\bar{u}_{II}^f = \sqrt{\frac{K_n^s}{K_t^s - A_t}}\, u_f \tag{41}$$

$$\bar{t}_{II} = \sqrt{\frac{K_n^s}{K_t^s - A_t}}\, K_t^s u_e$$

Finally, the mode I fracture energy can be computed as the normal separation work for $\gamma = \pi/2$, that is

$$G_I = W_n\left(\pi/2\right) = \frac{1}{2} K_n^s u_e u_f \tag{42}$$

whereas the tangential separation work is $W_t\left(\pi/2\right) = 0$. The mode II fracture energy is given by the tangential separation work for $\gamma = 0$, that is

$$G_{II} = W_t\left(0\right) = \frac{1}{2} K_n^s u_e u_f \frac{K_t^s}{K_t^s - A_t} = G_I \frac{K_t^s}{K_t^s - A_t} \tag{43}$$

and the normal separation work is $W_n\left(0\right) = 0$. Equation (43) confirms that for $A_t > 0$ mode II fracture energy is greater the the mode I value, $G_{II} > G_I$.

It can also be shown from Eqs. (39) that

$$W_n(\gamma) = G_I\, C^2(\gamma)\, \sin^2(\gamma); \qquad W_t(\gamma) = G_I\, \frac{K_t^s}{K_n^s} C^2(\gamma)\, \cos^2(\gamma); \tag{44}$$

and then

$$W(\gamma) = W_n(\gamma) + W_t(\gamma) = G_I\, C^2(\gamma) \left[\sin^2(\gamma) + \frac{K_t^s}{K_n^s}\, \cos^2(\gamma)\right]. \tag{45}$$

In Figures 4 the work of separation for the monotonic loading path is qualitatively represented as function of angle γ, where it can be observed that, for any mixed mode debonding condition, the separation work is

$$G_I \leq W\left(\alpha\right) \leq G_{II} \tag{46}$$

and it monotonically increases from the pure mode I condition to the pure mode II condition. Several experimental investigations confirm that fracture energy

18

in mixed mode debonding condition gradually and monotonically increases from the pure mode I value G_I to the pure mode II value G_{II}. Such a result is reported by Benzeggagh and Kenane (1996), who measured the fracture energy of a unidirectional glass/epoxy composite for six different mixed mode conditions, by the mixed mode bending apparatus developed by Crews and Reeder (1998)
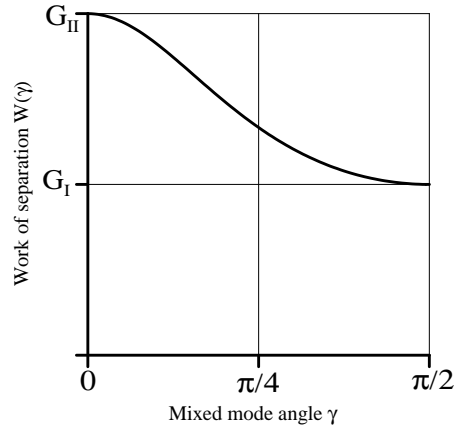

Figure 4: Work of separation in the monotonic loading path, in function of delamination angle γ.

4. Non-proportional loading paths

The behaviour of the proposed model is also analyzed for two non-proportional loading paths, well known in literature (van den Bosch et al., 2006; Park et al., 2009; Dimitri et al., 2014) for the validation of debonding models with different fracture energies in mode I and in mode II.

The first non-proportional loading path (a) is applied by an initial opening displacement, which increases up to a maximum value $u_n = u_{a1}$, and by a subsequent sliding displacement $u_t = u_{a2}$, which increases up to complete delamination.

The second non-proportional loading path (b) is applied by an initial sliding displacement, which increases up to a maximum value $u_t = u_{b1}$, and by

19

a subsequent opening displacement $u_n = u_{b2}$, which increases up to complete delamination. The two non-proportional loading paths are represented respectively in Fig.(5a) and in Fig.(5b).
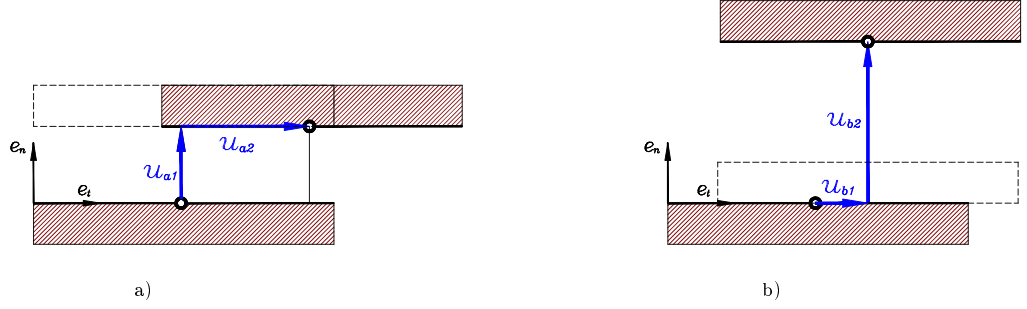

Figure 5: Non-proportional loading paths: a) path (a) opening displacement and subsequent sliding displacement; b) path (b) sliding displacement and subsequent opening displacement.

4.1. Non-proportional loading path (a)

The solution of non-proportional loading can be developed analytically and two different cases has to be distinguished:

- the initial normal displacement is less than or equal to the mode I limit elastic displacement ($u_{a1} \leq \bar{u}_I^e = u_e$);

- the initial normal displacement is greater than or equal to the mode I limit elastic displacement and less than the fully debonding displacement ($\bar{u}_I^e \leq u_{a1} < \bar{u}_I^f$).

In the first case, the normal displacement $u_n = u_{a1}$ produces elastic response and the second loading branch, with tangential displacement $u_t = u_{a2}$, is initially elastic. The first damage activation is reached at following tangential displacement

$$\bar{u}_t^e = \left[\frac{K_n^s}{K_t^s - A_t} \left(u_e^2 - u_{a1}^2 \right) \right]^{\frac{1}{2}} \tag{47}$$

20

and the fully debonding condition ($\omega = 1$) is reached at the following tangential displacement

$$\bar{u}_t^f = \left[\frac{K_n^s}{K_t^s - A_t} \left(u_f^2 - u_{a1}^2 \right) \right]^{\frac{1}{2}}.$$ (48)

The traction components after damage activation, for $\bar{u}_t^e \leq u_{a2} \leq \bar{u}_t^f$, are

$$t_n \left(u_{a1}, u_{a2} \right) = -\frac{u_e}{u_f - u_e} K_n^s u_{a1} + \frac{u_f}{u_f - u_e} K_n^s u_e u_{a1} \left[u_{a1}^2 + \frac{K_t^s - A_t}{K_n^s} u_{a2}^2 \right]^{-1/2}$$
$$t_t \left(u_{a1}, u_{a2} \right) = -\frac{u_e}{u_f - u_e} K_t^s u_{a2} + \frac{u_f}{u_f - u_e} K_t^s u_e u_{a2} \left[u_{a1}^2 + \frac{K_t^s - A_t}{K_n^s} u_{a2}^2 \right]^{-1/2}$$ (49)

The qualitatively behaviour of the proposed model, in terms of traction components *vs* separation displacements, for the non-proportional loading path (a) is represented in Fig.(6a) for an initial normal displacement less than the mode I elastic limit value $\left(u_n^{a1} \leq \bar{u}_I^e = u_e \right)$.
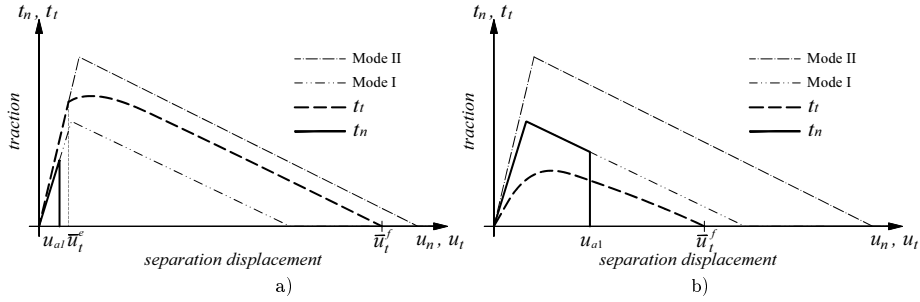

Figure 6: Non-proportional loading path (a): a) initial normal displacement less than the mode I elastic limit value $\left(u_{a1} \leq \bar{u}_I^e \right)$; b) initial normal displacement greater than the mode I elastic limit value $\left(\bar{u}_I^e \leq u_{a1} < \bar{u}_I^f \right)$.

Finally, the work done by normal traction, the work done by tangential traction and total work-of-separation, respectively, are

$$W_n = \frac{1}{2} K_n^s u_{a1}^2$$
$$W_t = \frac{1}{2} K_t^s \bar{u}_t^{e\,2} + \int_{\bar{u}_t^e}^{\bar{u}_t^f} t_t \, \mathrm{d}u_t = G_{II} - \frac{K_t^s}{K_t^s - A_t} \frac{1}{2} K_n^s u_{a1}^2$$ (50)
$$W = W_n + W_t = G_{II} - \frac{A_t}{K_t^s - A_t} \frac{1}{2} K_n^s u_{a1}^2.$$

21

The second case of non-proportional loading path (a) is obtained with an initial normal displacement greater than or equal to the mode I limit elastic value and less than the fully debonding displacement ($\bar{u}_I^e \leq u_{a1} < \bar{u}_I^f$). The damage value at the end of the first loading branch ($u_n = u_{a1}, u_t = 0$) is

$$\omega\left(u_{a1}, 0\right) = \frac{u_f}{u_f - u_e}\frac{u_{a1} - u_e}{u_{a1}} \tag{51}$$

and the relevant traction components are

$$t_n\left(u_{a1}, 0\right) = k_n^s u_e \frac{u_f - u_{a1}}{u_f - u_e}$$
$$t_t\left(u_{a1}, 0\right) = 0. \tag{52}$$

The behaviour in the second loading branch ($u_n = u_{a1}, u_t = u_{a2}$) is completely nonlinear and the traction components are given by Eqs. (49a, b). The tangential displacement at the fully debonded condition is again given by Eq. (48), obtained for the first case.

The qualitatively behaviour of the proposed model, in terms of traction components *vs* separation displacements, for the non-proportional loading path (a) is represented in Figure (6b) for an initial normal displacement greater than the mode I elastic limit value ($\bar{u}_I^e \leq u_{a1} < \bar{u}_I^f$).

Finally, the work done by normal traction, the work done by tangential traction and total work-of-separation, respectively, are

$$W_n = \int_0^{u_{a1}} t_n du_n = G_I - G_I \frac{(u_f - u_{a1})^2}{u_f(u_f - u_e)}$$
$$W_t = \int_0^{\bar{u}_t^f} t_t du_t = G_{II} \frac{(u_f - u_{a1})^2}{u_f(u_f - u_e)} \tag{53}$$
$$W = W_n + W_t = G_I + (G_{II} - G_I)\frac{(u_f - u_{a1})^2}{u_f(u_f - u_e)}.$$

4.2. Non-proportional loading path (b)

The non-proportional loading path (b) is schematically represented in Fig. (5b) and it imposes an initial tangential displacement u_{b1} and than a monotonically increasing normal displacement u_{b2} is applied up to the fully debonding.

Similar to the previous loading path (a), the analytical solution of the loading path (b) has to be developed for two different cases:

22

- the initial tangential displacement is less than or equal to the mode II limit elastic displacement ($u_{b1} \leq \bar{u}_{II}^e$);

- the initial tangential displacement is greater than or equal to the mode II limit elastic displacement and less than the fully debonding displacement ($\bar{u}_{II}^e \leq u_{b1} < \bar{u}_{II}^f$).

In the first case, the tangential displacement u_{b1} produces elastic response and the second loading branch, with normal displacement u_{b2}, is initially elastic. The first damage activation is reached at following normal displacement

$$\bar{u}_n^e = \left[\bar{u}_I^{e\,2} - \frac{K_t^s - A_t}{K_n^s} u_{b1}^2\right]^{\frac{1}{2}} \tag{54}$$

while the fully debonding condition ($\omega = 1$) is reached at normal displacement

$$\bar{u}_n^f = \left[\bar{u}_I^{f\,2} - \frac{K_t^s - A_t}{K_n^s} u_{b1}^2\right]^{\frac{1}{2}}. \tag{55}$$

Traction components after damage activation, for $\bar{u}_n^e \leq u_{b2} \leq \bar{u}_n^f$, are

$$
\begin{aligned}
t_n\left(u_{b2}, u_{b1}\right) &= -\frac{u_e}{u_f - u_e} K_n^s u_{b2} + \frac{u_f}{u_f - u_e} K_n^s u_{b2} u_e \left[u_{b2}^2 + \frac{K_t^s - A_t}{K_n^s} u_{b1}^2\right]^{-\frac{1}{2}} \\
t_t\left(u_{b2}, u_{b1}\right) &= -\frac{u_e}{u_f - u_e} K_t^s u_{b1} + \frac{u_f}{u_f - u_e} K_t^s u_{b1} u_e \left[u_{b2}^2 + \frac{K_t^s - A_t}{K_n^s} u_{b1}^2\right]^{-\frac{1}{2}}
\end{aligned}
\tag{56}
$$

The qualitatively behaviour of the proposed model, in terms of traction components *vs* separation displacements, for the non-proportional loading path (b) is represented in Figure (7a) for an initial tangential displacement less than the mode II elastic limit value ($u_{b1} \leq \bar{u}_{II}^e$).

Finally, the work done by normal traction, the work done by the tangential one and the total work-of-separation, respectively, are

$$
\begin{aligned}
W_n &= \frac{1}{2} K_n^s \bar{u}_n^{e\,2} + \int_{\bar{u}_n^e}^{\bar{u}_n^f} t_n \, \mathrm{d}u_n = G_I - \frac{1}{2}(K_t^s - A_t) u_{b1}^2 \\
W_t &= \frac{1}{2} K_t^s u_{b1}^2 \\
W &= W_n + W_t = G_I + \frac{1}{2} A_t u_{b1}^2.
\end{aligned}
\tag{57}
$$

The second case of non-proportional loading path (b) is obtained with an initial tangential displacement greater than or equal to the mode II limit elastic

23

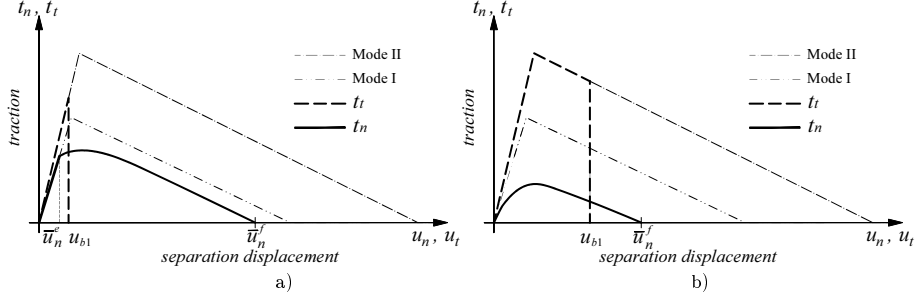Figure 7: Non-proportional loading path (b): a) initial tangential displacement less than the mode II elastic limit value ($u_{b1} \leq \bar{u}_{II}^e$); b) initial tangential displacement greater than the mode II elastic limit value ($\bar{u}_{II}^e \leq u_{b1} < \bar{u}_{II}^f$).

value and less than the fully debonding displacement ($\bar{u}_{II}^e \leq u_{b1} < \bar{u}_{II}^f$). The damage value at the end of the first loading branch ($u_n = 0, u_t = u_{b1}$) is

$$\omega\left(0, u_{b1}\right) = \frac{u_f}{u_f - u_e} \frac{u_{b1} - \bar{u}_{II}^e}{u_{b1}} \tag{58}$$

and the relevant traction components are

$$\begin{aligned} t_n\left(0, u_{b1}\right) &= 0 \\ t_t\left(0, u_{b1}\right) &= K_t^s \bar{u}_{II}^e \frac{\bar{u}_{II}^f - u_{b1}}{\bar{u}_{II}^f - \bar{u}_{II}^e}. \end{aligned} \tag{59}$$

The behavior in the second loading branch ($u_n = u_{b2}, u_t = u_{b1}$) is completely nonlinear and the traction components are defined by the same relations of previous case, that are given by Eqs. (56 a, b). The tangential displacement at the fully debonded condition is again given by Eq. (55), obtained for the first case.

The qualitatively behavior of the proposed model, in terms of traction components vs separation displacements, for the non-proportional loading path (b) is represented in Figure (7b) for an initial tangential displacement greater than the mode II elastic limit value ($\bar{u}_{II}^e \leq u_{b1} < \bar{u}_{II}^f$).

Finally, the work done by normal traction, the work done by tangential

24

444 traction and total work-of-separation, respectively, are

$$W_n = \int_0^{\bar{u}_n^f} t_n \, \mathrm{d}u_n = G_I \frac{\left(\bar{u}_{II}^f - u_{b1}\right)^2}{\bar{u}_{II}^f \left(\bar{u}_{II}^f - \bar{u}_{II}^e\right)}$$

$$W_t = \int_0^{\bar{u}_t^f} t_t \, \mathrm{d}u_t = G_{II} - G_{II} \frac{\left(\bar{u}_{II}^f - u_{b1}\right)^2}{\bar{u}_{II}^f \left(\bar{u}_{II}^f - \bar{u}_{II}^e\right)} \qquad (60)$$

$$W = W_n + W_t = G_{II} + (G_I - G_{II}) \frac{\left(\bar{u}_{II}^f - u_{b1}\right)^2}{\bar{u}_{II}^f \left(\bar{u}_{II}^f - \bar{u}_{II}^e\right)}.$$

445 The work done by the normal traction, the work done by the tangential one and

446 the total work-of-separation, performed in the non-proportional loading path

447 (a), are plotted in Figure (8) in function of the initial normal displacement u_{a1}.

448 The work done by the normal traction, the work done by the tangential one and

449 the total work-of-separation, performed in the non-proportional loading path

450 (b), are plotted in Figure. (9) in function of the initial tangential displacement

451 u_{b1}.

452 The results plotted in the Figs. (8) and (9) have been evaluated with the

453 following constitutive parameters: $k_n^s = k_t^s = 1000 N/mm^3$, $A_t = 500 N/mm^3$,

454 $u_e = 0.005mm$, $u_f = 0.04mm$; which produces the mode I fracture energy $G_I =$

455 $0.1 N/mm = 100 J/m^2$ and the mode II fracture energy $G_{II} = 0.2 N/mm =$

456 $200 J/m^2$. Moreover, displacements at the initial damage condition and at

457 the fully debonded one, in pure mode I loading law, are: $\bar{u}_I^e = 0.005mm$,

458 $\bar{u}_I^f = 0.04mm$; and in pure mode II loading law: $\bar{u}_{II}^e = 0.00707mm$, $\bar{u}_{II}^f =$

459 $0.05657mm$.

460 The graphs in Figures (8) and (9) show the path dependency of work-of-

461 separation and, especially, its smooth and monotonic transition from the mode

462 I fracture energy G_I to the mode II fracture energy G_{II} and *vice versa*.

463 For the first non-proportional loading path (Figure 5 a), a null initial nor-

464 mal displacement $u_{a1} = 0$ produces a pure mode II failure and, as shown in

465 Figure (8), the total work-of-separation is $W = W_t = G_{II}$ and work done by

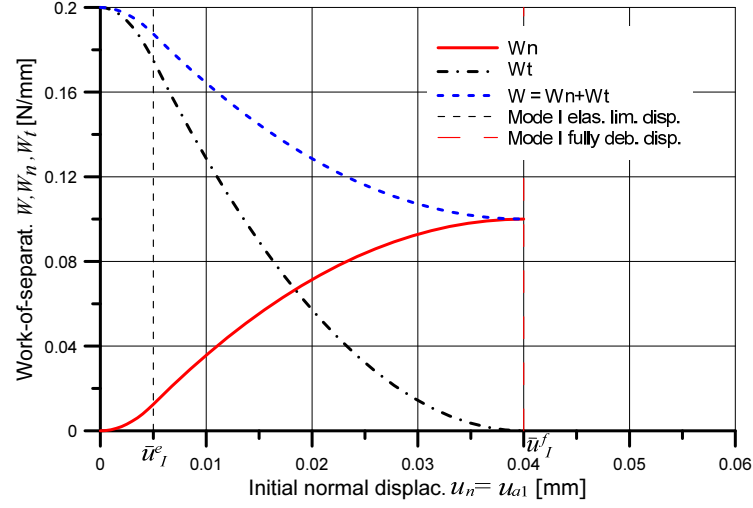**466** normal traction is $W_n = 0$. On the contrary, the initial normal displacement

25

Figure 8: Work done by the normal traction, work done by the tangential traction and the total work-of-separation, performed in the non-proportional loading path (a).
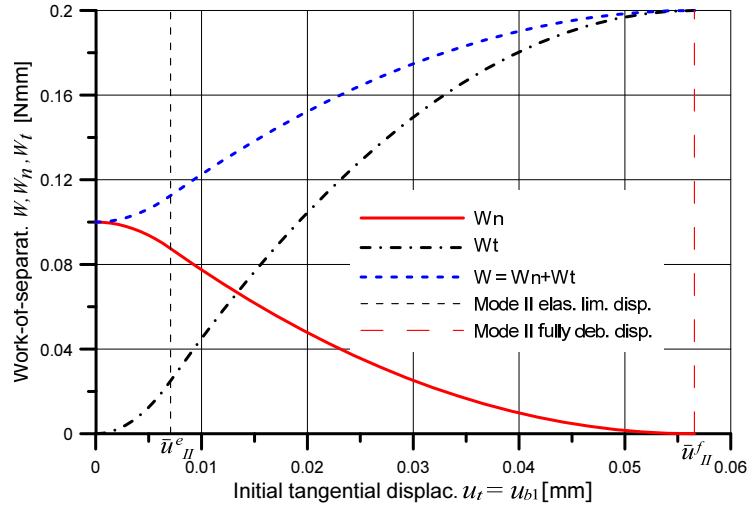

Figure 9: Work done by the normal traction, work done by the tangential traction and the total work-of-separation, performed in the non-proportional loading path (b).

467 $u_{a1} = \bar{u}_I^f$ produces a pure mode I failure and the total work-of-separation is

468 $W = W_n = G_I$ and work done by tangential traction is $W_t = 0$, as con-

469 firmed in Figure (8). In Figure (8), the other values of the normal displacement

470 $0 < u_{a1} < \bar{u}_I^f$ produce mixed mode failure conditions with smooth and mono-

471 tonic variation of normal work W_n, tangential work W_t and total work W from

472 the pure mode II condition to the pure mode I condition.

473   Analogous results can be observed in Figure (9) for the second non-proportional

474 loading path (Figure 5 b), where an initial tangential displacement $u_{b1} = 0$ pro-

475 duces a pure mode I failure and $u_{b1} = \bar{u}_{II}^f$ produces a pure mode II failure.

476   In Dimitri et al. (2014) the response to the non-proportional loading paths

477 (a) and (b) of some interface constitutive models (van den Bosch et al., 2006;

478 McGarry et al., 2014; Högberg, 2006; Camanho et al., 2003) are reported in

479 terms of total work-of-separation, work done by normal traction and work done

480 by tangential traction, as function of the ratios $u_{a1}/\bar{u}_I^f$ for the path (a) and as

481 function of the ratios $u_{b1}/\bar{u}_{II}^f$ for the path (b).

482   In order to compare the proposed model with models available in literature,

483 the results of the two non-proportional loading paths (a) and (b) plotted in

484 Figures (8) and (9) are based on the same values of mode I fracture energy G_I

485 and mode II fracture energy G_{II} assumed in Dimitri et al. (2014).

486   Several CZMs proposed in literature (Xu and Needleman, 1993; Högberg,

487 2006; Camanho et al., 2003) are inaccurate in mixed mode failure conditions (see

488 Dimitri et al. (2014) for a comparative analysis), producing work-of-separation

489 less than mode I fracture energy ($W < G_I$) or greater than mode II fracture

490 energy ($W > G_{II}$). On the contrary, the CZMs proposed in van den Bosch et al.

491 (2006); Dimitri et al. (2014); Park et al. (2009) produce normal work, tangential

492 work and total work-of-separation qualitatively similar to the results plotted

493 respectively, in Figure (8) for the first non-proportional loading path and in

494 Fig.(9) for the second non-proportional loading path. However, CMZs proposed

495 in van den Bosch et al. (2006); Park et al. (2009) are not based on an Helmholtz

496 free energy and are not thermodynamically consistent; the CZM proposed in

497 Dimitri et al. (2014) is fully thermodynamically consistent, but it is based on

27

four scalar damage variable, whose physical or mechanical interpretation is not evident. Moreover, such model does not allows to consider frictional effects on the damaged fraction, by the mesoscale interpretation proposed in Parrinello et al. (2009) and Alfano and Sacco (2006).

5. Numerical simulation

The proposed model has been implemented in the finite element code FEAP (Zienkiewicz and Taylor, 2000) and three different delamination tests have been numerically simulated, namely:

- end-notched double cantilever beam test;

- a mixed mode bending test on end-notched specimen.

- a four points end-notched flexural delamination test;

The numerical simulations have been performed using 2D nine nodes plane stress elements and six nodes interface elements. The bulk is modeled as isotropic and linear elastic with Young modulus $E = 35300\,N/mm^2$ and Poisson ratio $\nu = 0.3$ (standard parameters for E-glass/epoxy composite material). Two different sets of interface constitutive parameters have been considered, both with the same fracture energies ($G_I = 1N/mm$ and $G_{II} = 4N/mm$) but with different normal tensile strength and shear strength. The first set is reported in Table 1 and produces normal tensile strength $\bar{t}_I = 20\,N/mm^2$ and shear strength $\bar{t}_{II} = 40\,N/mm^2$, whereas the second set of constitutive parameters produces normal tensile strength $\bar{t}_I = 40\,N/mm^2$ and shear strength $\bar{t}_{II} = 80\,N/mm^2$

The analytical solutions of the three delamination tests are known in literature and developed in the framework of classical linear elastic fracture mechanics coupled with bending beam theory.

5.1. DCB test

Sizes and geometry of analyzed specimen are represented in Fig.10 and the analytical response, under bending beam theory and linear fracture mechanics

28

	Cohesive Parameters
Normal elastic stiffness	$K_n^s = 50\,000\,N/mm^3$
Tangential elastic stiffness	$K_t^s = 50\,000\,N/mm^3$
Mixed mode parameter	$A_t = 37\,500\,N/mm^3$
Mode I elastic displ.	$\bar{u}_I^e = u_e = 0.0004\,mm$
Mode I debonding displ.	$\bar{u}_I^f = u_f = 0.1\,mm$
Tensile strength	$\bar{t}_I = 20\,N/mm^2$
Mode II elastic displ.	$\bar{u}_{II}^e = 0.0008\,mm$
Mode II debonding displ.	$\bar{u}_{II}^f = 0.2\,mm$
Shear strength	$\bar{t}_{II} = 40\,N/mm^2$
Mode I Fracture energy	$G_I = 1\,N/mm$
Mode II Fracture energy	$G_{II} = 4\,N/mm$
	Frictional Parameters
Normal elastic stiffness	$K_n^f = 50\,000\,N/mm^3$
Tangential elastic stiffness	$K_t^f = 5\,000\,N/mm^3$
Frictional coefficient	$\alpha = 0.8391$
Dilatancy coefficient	$\beta = 0$

Table 1: Model constitutive parameters used for the numerical simulations.

theory is given, in terms of imposed displacement u and relevant load P, by

$$u = 4a^2 \sqrt{\frac{G_I}{3Eh^3}}$$
$$P = \frac{3EI}{2a^3} u$$

(61)

with $I = bh^3/12$. Results of numerical simulation are plotted in Fig.11 in terms of horizontal normal stress at the initial delamination condition. Results of analytical solution and numerical simulations are compared in Figure 12. The numerical results properly reproduce the analytical solution in the descending branch, whereas the numerical solution is less stiff than the analytical one in the initial elastic path. In fact the analytical solution is based on the linear elastic fracture mechanics theory, which assumes an ideally brittle traction-separation

29

533 law. As a consequence, the initially elastic behaviour of the interface produces

534 a less stiff response.

535   The initial elastic behaviour assumed for the interface can be considered

536 as a penalty approach in order to impose the rigidity constrain. The interface

537 elastic stiffness, or equivalently the tensile strength $\bar{t}_I$ for fixed fracture energy,

538 represents the penalty parameter. Is well known that analytical solution can

539 not be caught by penalty method and, as penalty parameter increases over a

540 specific value, error in numerical solution increases too. Such a problem has

541 been observed in the numerical solution of the DBC test for $\bar{t}_I > 40 \, N/mm^2$.
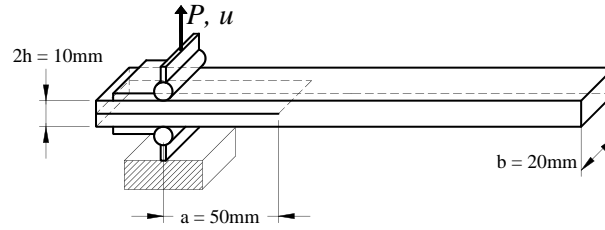
Figure 10: Sizes and geometry of specimen for the double cantilever beam test.
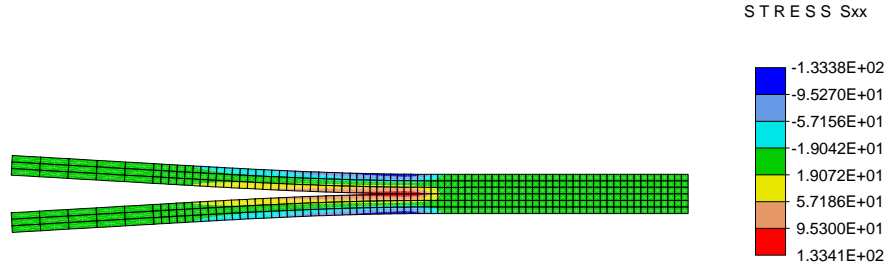
Figure 11: Map of normal stress Sxx obtained by the numerical simulation of the double cantilever beam test at the initial delamination condition.

542 *5.2. MMB test*

543   The second numerical simulation is the mixed mode bending test of an end

544 notched specimen, performed by the apparatus developed by Reeder and Crews

545 (1990). The MMBT has been standardized by ASTM (2006). The mixed mode

546 bending apparatus is represented in Fig.13, with sizes and geometry of specimen,
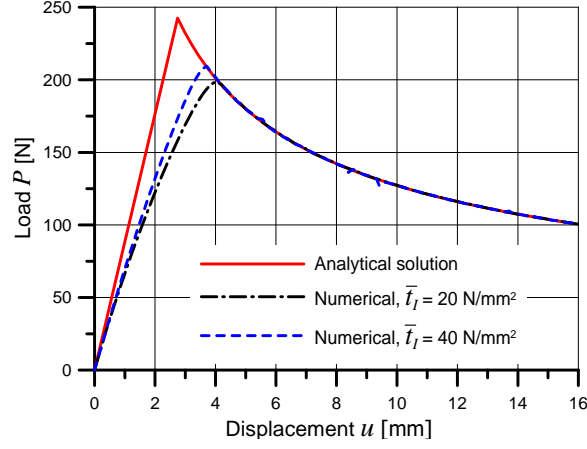
547 boundary conditions and applied load.

Figure 12: Response of double cantilever beam test, in terms of applied load vs imposed displacement. Analytical solution and numerical solutions with two different tensile strengths.

The analytical solution is defined in terms of crack opening displacement d (see Figure 13) and applied load P, and it is derived in the framework of fracture mechanics and beam theory. Analytical solution at the first delamination, for crack length less than the beam half-span ($a \leq L$), is given in Mi et al. (1998) as

$$
\begin{aligned}
P &= \frac{1}{a}\sqrt{\frac{8EIb}{\frac{8}{G_I}\left(\frac{3C-L}{4L}\right)^2 + \frac{3}{8G_{II}}\left(\frac{C+L}{L}\right)^2}} \\
d &= \frac{2Pa^3}{3EI}\frac{3C-L}{4L}
\end{aligned}
\tag{62}
$$

with $I = bh^3/12$. The second analytical solution, for crack extended behind the beam mid-span ($a \geq L$), was initially given in Mi et al. (1998), but a corrected formulation was proposed in Tenchev and Falzon (2007) in term of crack opening displacement

$$
d = \frac{P}{EI}\frac{\left(a^3 + 3a^2L - L^3\right)(L+C) - 4a^3L}{6L}
\tag{63}
$$

and the applied load can be derived by the following mixed mode interaction fracture criterion

$$
\frac{Y_I}{G_I} + \frac{Y_{II}}{G_{II}} = 1
\tag{64}
$$

31

where Y_I and Y_{II} are the following energy release rates

$$Y_I = \frac{P^2 L^2}{8bEI} \left[\frac{a^2}{2L^2} \left(\frac{C}{L} - 3 \right)^2 + \frac{a}{2L} \left(\frac{C}{L} + 1 \right) \left(5\frac{C}{L} - 13 \right) + \left(\frac{C}{L} + 1 \right) \left(\frac{C}{L} + 3 \right) \right]$$

$$Y_{II} = \frac{P^2 L^2}{8bEI} \left[\frac{3a^2}{8L^2} \left(\frac{C}{L} + 1 \right)^2 - \frac{a}{L} \left(\frac{C}{L} + 1 \right) \left(2\frac{C}{L} + 1 \right) + \frac{1}{2} \left(\frac{C}{L} + 1 \right) \left(5\frac{C}{L} + 1 \right) \right].$$

(65)

The results of numerical simulations, performed with the two sets of consti-
tutive parameters, are compared to the analytical solution in Fig.15, in terms of
applied load vs crack opening displacement. Good agreement between numer-
ical and analytical results can be observed. Map of tangential stress obtained
by the numerical simulation, at the loading condition of imposed displacement
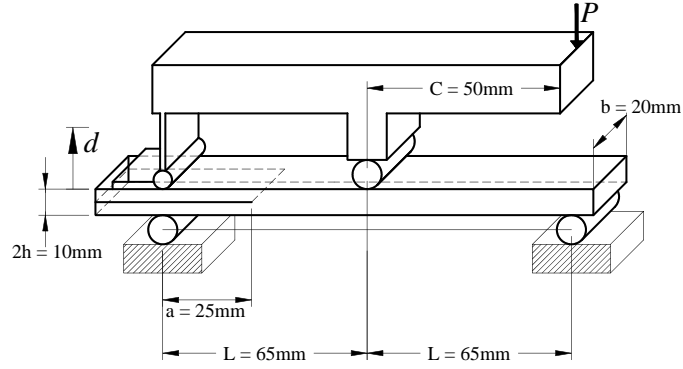$u = 1mm$, is plotted in Fig.14.

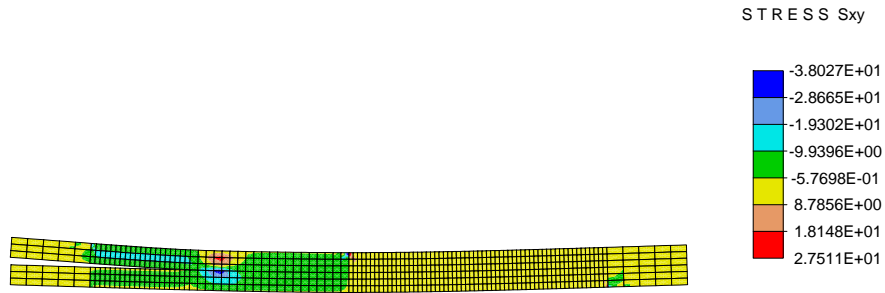Figure 13: Sizes and geometry of specimen for the mixed mode test (MMBT).

Figure 14: Map of tangential stress Sxy obtained by the numerical simulation of the MMBT at the loading condition of imposed displacement $u = 1mm$.
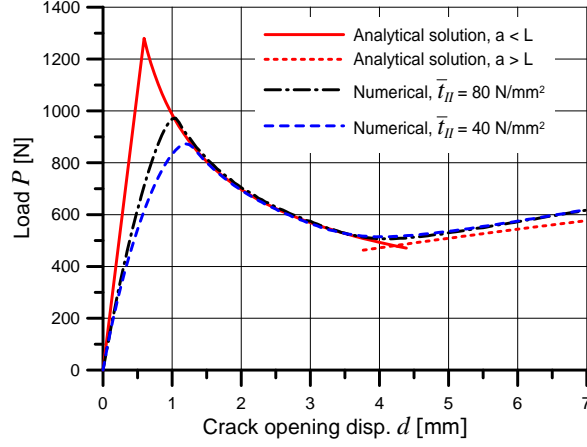
Figure 15: Response of mixed mode bending test, in terms of applied load vs crack opening displacement. Analytical solution and numerical solutions with two different tensile strengths.

5.3. 4ENF test

The third numerical simulation is the four points bend end-notched flexure test (4ENF), represented in Figure 16 with the relevant sizes.

The analytical solution can be developed in the framework of beam theory and fracture mechanics (Martin and Davidson, 1999) and is given by

$$
\begin{aligned}
P &= \frac{4}{3}\frac{B}{L-D}\sqrt{E\,h^3\,G_{II}} \\
u &= P\frac{(L-D)^2}{24EI}(3a+4D-2L)
\end{aligned}
\tag{66}
$$

with $I = bh^3/12$. Map of tangential stress obtained by the numerical simulation, at the loading condition of imposed displacement $u = 3mm$, is plotted in Fig.17. Results of numerical simulation and analytical solution are compared in Figure 18 in terms of applied load P and relevant displacement u, for both the two set of constitutive parameters. Moreover, two solutions with positive frictional coefficients have been carried out and results are compared to the analytical (frictionless) solution.

4ENF test is known in literature (Schuecker and Davidson, 2000) for its accuracy on the determination of mode II delamination toughness, which is influenced by frictional effects, over than by ratio between inner span and outer
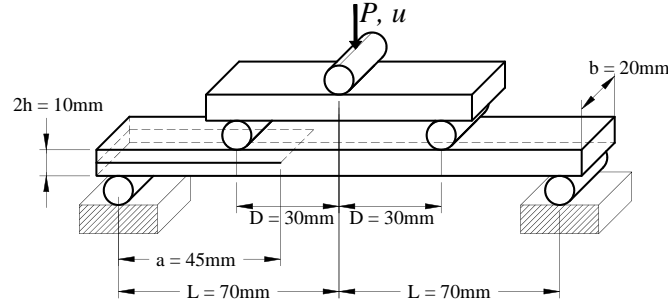
33

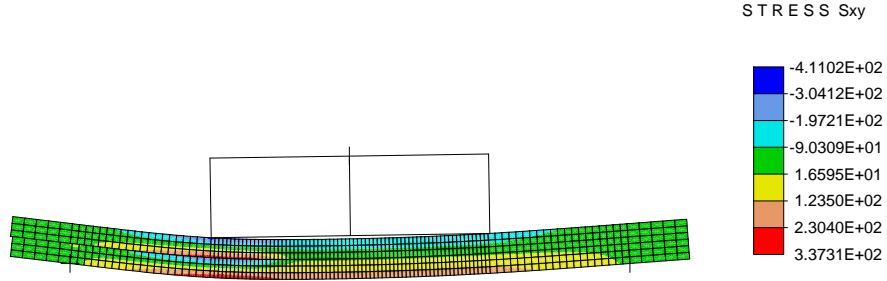Figure 16: Sizes and geometry of specimen for the four point bend end-notched flexure test (4ENF).

Figure 17: Map of tangential stress Sxy obtained by the numerical simulation of the 4ENF at the loading condition of imposed displacement $u = 3mm$.
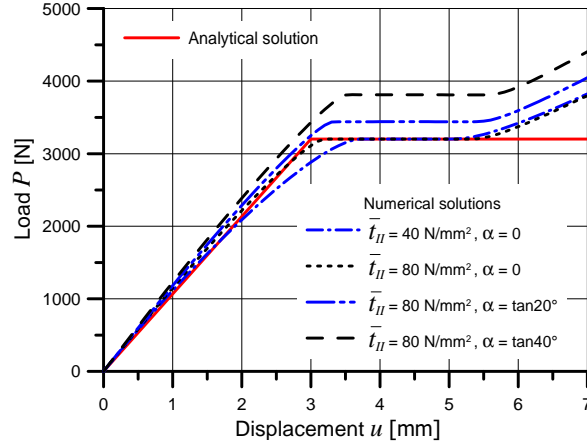

Figure 18: Response of 4ENF test, in terms of applied load vs imposed displacement. Analytical solution and numerical solutions with two different tensile strengths and with three different frictional coefficients.

34

span (D/L with reference to Fig.16).

The proposed model can numerically reproduce the standard 4PBT and it can also take into account the presence of frictional effects. Numerical simulations with two frictional coefficients ($\alpha = \tan 20^o$ and $\alpha = \tan 40^o$) and null dilatancy coefficient ($\beta = 0$) have been performed and results are shown in Fig.18 and compared the frictionless numerical results and with analytical solution. Diagrams plotted if Fig. 18 show that applied load at delamination condition is 7.5% greater than frictionless response, for the frictional coefficient $\alpha = \tan 20^o$, and 19% greater than frictionless response, for the frictional coefficient $\alpha = \tan 40^o$.

Finally, the differences between numerical and analytical responses in the initial elastic branch, observable in the three delamination tests, are intrinsic to the cohesive zone formulations. In fact, the analytical solution are developed in the linear fracture mechanics, for which the behaviour is linear elastic up to delamination starts. On the contrary, in cohesive zone models the delamination phenomenon is subsequent the nonlinear behaviour in the cohesive zone and the response is less stiff than the analytical one.

6. Closing remarks

The paper presents as a main innovative finding an interface unified constitutive framework based on a single damage variable in a thermodynamic consistent context, which has a proper free energy, dissipation function, activation function and evolution rules, all derived in the context of dissipative mechanics with internal variables.

The proposed CZM, produces two independent fracture energies, G_I in pure mode I debonding condition and G_{II} in pure mode II debonding one. G_I and G_{II}, as analytically shown, are minimum and maximum values of the work-of-separation for any proportional and non-proportional loading paths. The model can also evaluates the presence of frictional tractions both at the fully debonded zones and at the partially debonded ones.

35

The proposed model is able to accurately reproduce with a unique set of few constitutive parameters, very different and general proportional and non-proportional, monotonic and cyclic, loading paths, either in opening mode or in sliding mode and in any mixed condition, recovering also closing conditions and frictional effects.

Finally, three classical delamination tests (DBC, MMB, 4ENF) have been numerically reproduced and the results compared with the analytical ones, showing good agreement.

Acknowledgment

References

Alfano, G., Crisfield, M., 2001. Finite element interface models for the delamination analysis of laminated composites: Mechanical and computational issues. Int. J. Num. Meth. Eng. 50 (7), 1701–1736.

Alfano, G., Sacco, E., 2006. Combining interface damage and friction in a cohesive-zone model. Int. J. Num. Meth. Eng. 68 (5), 542–582.

Allix, O., Ladevĩl̃ze, P., Corigliano, A., 1995. Damage analysis of interlaminar fracture specimens. Comp. Struct. 31 (1), 61–74.

ASTM, 2006. Standard test method for mixed mode i-mode ii interlaminar fracture toughness of unidirectional fiber reinforced polymer matrix composites: Technical report astm d6671/d6671m. Tech. rep., ASTM International.

Barenblatt, G., 1962. The mathematical theory of equilibrium cracks in brittle fracture. Advances in Applied Mechanics 7, 55–129.

637 Benzeggagh, M. L., Kenane, M., 1996. Measurement of mixed-mode delamina-
638 tion fracture toughness of unidirectional glass/epoxy composites with mixed-
639 mode bending apparatus. Compos. Sci. Technol. 56, 439–449.

640 Benzerga, D., Haddi, A., Seddak, A., Lavie, A., 2008. A mixed-mode damage
641 model for delamination growth applied to a new woven composite. Comp.
642 Mat. Sci. 41 (4), 515–521.

643 Camanho, P., DÃ₂vila, C., De Moura, M., 2003. Numerical simulation of mixed-
644 mode progressive delamination in composite materials. J. Comp. Materials
645 37 (16), 1415–1438.

646 Coleman, B., Noll, W., 1963. The thermodynamics of elastic materials with heat
647 conduction and viscosity. Arch. Rat. Mech. Analysis 13, 167–178.

648 Corigliano, A., 1993. Formulation, identification and use of interface models in
649 the numerical analysis of composite delamination. Int. J. Solids Structures
650 30 (20), 2779–2811.

651 Corigliano, A., Allix, O., 2000. Some aspects of interlaminar degradation in
652 composites. Comp. Meth. Appl. Mech. Eng. 185 (2-4), 203–224.

653 Corigliano, A., Ricci, M., 2001. Rate-dependent interface models: Formulation
654 and numerical applications. Int. J. Solids Structures 38 (4), 547–576.

655 Crews, J., Reeder, J., 1998. A mixed-mode bending apparatus for delamination
656 testing, technical memorandum 100662. Tech. rep., NASA Lagley.

657 Daudeville, L., Allix, O., Ladevéze, P., 1995. Delamination analysis by damage
658 mechanics: Some applications. Comp. Engng 5 (1), 17–24.

659 Dimitri, R., Trullo, M., Zavarise, G., De Lorenzis, L., 2014. A consistency assess-
660 ment of coupled cohesive zone models for mixed-mode debonding problems.
661 Frattura ed Integrita Strutturale 8 (29), 266–283.

662 Dugdale, D., 1960. Yielding of steel sheets containing slits. J. Mech. Phys. Solids.
663 8, 100–104.

Ganghoffer, J., Schultz, J., 1997. Interactions between adhesion and friction—i. theoretical aspects. J. Mech. Phy. Solids 45 (1), 151–174.

Giambanco, G., Fileccia Scimemi, G., 2006. Mixed mode failure analysis of bonded joints with rate-dependent interface models. Int. J. Num. Meth. Engng. 67 (8), 1160–1192.

Guiamatsia, I., Nguyen, G., 2014. A thermodynamics-based cohesive model for interface debonding and friction. Int. J. Solids Structures 51 (3-4), 647–659.

Högberg, J., 2006. Mixed mode cohesive law. Int. J. Fracture 141 (3-4), 549–559.

Kolluri, M., Hoefnagels, J. P. M., van Dommelen, J. A. W., Geers, M. G. D., 2014. Irreversible mixed mode interface delamination using a combined damage-plasticity cohesive zone enabling unloading. Int. J. Fracture 185, 77–95.

Martin, R., Davidson, B., 1999. Mode ii fracture toughness evaluation using four point bend, end notched flexure test. Plas. Rubber Compos. Proc. Appl. 28 (8), 401–406.

McGarry, J., Ó Máirtín, ., Parry, G., Beltz, G., 2014. Potential-based and non-potential-based cohesive zone formulations under mixed-mode separation and over-closure. part i: Theoretical analysis. J. Mech. Physics Solids 63 (1), 336–362.

Mi, Y., Crisfield, M., Davies, G., Hellweg, H.-B., 1998. Progressive delamination using interface elements. J. Compos. Materials 32 (14), 1246–1272.

Mosler, J., Scheider, I., 2011. A thermodynamically and variationally consistent class of damage-type cohesive models. J. Mech. Physics Solids 59 (8), 1647–1668.

Musto, M., Alfano, G., 2013. A novel rate-dependent cohesive-zone model combining damage and visco-elasticity. Computers and Structures 118, 126–133.

690 Park, K., Paulino, G., Roesler, J., 2009. A unified potential-based cohesive
691   model of mixed-mode fracture. J. Mech. Physics Solids 57 (6), 891–908.

692 Parrinello, F., Failla, B., Borino, G., 2009. Cohesive-frictional interface consti-
693   tutive model. Int. J. Solids Structures 46 (13), 2680–2692.

694 Parrinello, F., Marannano, G., Borino, G., Pasta, A., 2013. Frictional effect
695   in mode ii delamination: Experimental test and numerical simulation. Eng.
696   Fract. Mech. 110, 258–269.

697 Reeder, J., Crews, J., 1990. Mixed-mode bending method for delamination test-
698   ing. AIAA Journal 28, 1270–1276.

699 Sacco, E., Lebon, F., 2012. A damage-friction interface model derived from
700   micromechanical approach. Int. J. Solids Structures 49 (26), 3666–3680.

701 Schuecker, C., Davidson, B., 2000. Evaluation of the accuracy of the four-point
702   bend end-notched flexure test for mode ii delamination toughness determina-
703   tion. Compos. Sci. Tech. 60 (11), 2137–2146.

704 Serpieri, R., Alfano, G., 2011. Bond-slip analysis via a thermodynamically con-
705   sistent interface model combining interlocking, damage and friction. Int. J.
706   Num. Meth. Engng. 85 (2), 164–186.

707 Serpieri, R., Sacco, E., Alfano, G., 2015. A thermodynamically consistent deriva-
708   tion of a frictional-damage cohesive-zone model with different mode i and
709   mode ii fracture energies. Eur. J. Mech., A/Solids 49, 13–25.

710 Spada, A., Giambanco, G., Rizzo, P., 2009. Damage and plasticity at the inter-
711   faces in composite materials and structures. Comp. Meth. Appl. Mech. Eng.
712   198 (49-52), 3884–3901.

713 Tenchev, R., Falzon, B., 2007. A correction to the analytical solution of the
714   mixed-mode bending (mmb) problem. Compos. Sci. Tech. 67 (3-4), 662–668.

715 van den Bosch, M., Schreurs, P., Geers, M., 2006. An improved description of the
716   exponential xu and needleman cohesive zone law for mixed-mode decohesion.
717   Eng. Fract. Mech. 73 (9), 1220–1234.

718 Xu, X. P., Needleman, A., 1993. Void nucleation by inclusion debonding in a
719   crystal matrix. Modell. Simulation Mater. Sci. Eng. 2, 417–418.

720 Zienkiewicz, O., Taylor, 2000. The Finite Element Method. 5th Edition.
721   Butterworth-Heinemann Press.

722 Zreid, I., Fleischhauer, R., Kaliske, M., 2013. A thermomechanically coupled
723   viscoelastic cohesive zone model at large deformation. Int. J. Solids Structures
724   50, 4279–4291.